Journal of Colloid and Interface Science 434 (2014) 28–39

Contents lists available at ScienceDirect

Journal of Colloid and Interface Science

www.elsevier.com/locate/jcis

Interfacial phenomena at a surface of partially silylated nanosilica

V.M. Gun'ko [a,*], V.V. Turov [a], I.F. Myronyuk [b], O.V. Goncharuk [a], E.M. Pakhlov [a], N.A. Bezruka [b], E. Skwarek [c], W. Janusz [c], J.P. Blitz [d]

[a] Chuiko Institute of Surface Chemistry, 17 General Naumov Street, 03164 Kyiv, Ukraine
[b] Vasyl Stefanyk Precarpathian National University, 57 Shevchenko Street, 76018 Ivano-Frankovsk, Ukraine
[c] Faculty of Chemistry, Maria Curie-Skłodowska University, 20-031 Lublin, Poland
[d] Eastern Illinois University, Department of Chemistry, Charleston, IL 61920, USA

ARTICLE INFO

Article history:
Received 13 July 2014
Accepted 4 August 2014
Available online 14 August 2014

Keywords:
Partially silylated nanosilica
Water–methane co-adsorption
Water–hydrogen co-adsorption
Dispersion medium effects

ABSTRACT

Unmodified pyrogenic silica PS300 and partially silylated nanosilica samples at a degree of substitution of surface silanols by trimethylsilyl (TMS) groups Θ_{TMS} = 27.2% and 37.2% were studied to elucidate features of the interfacial behavior of water adsorbed alone, or co-adsorbed with methane, hydrogen, or trifluoroacetic acid (TFAA). In the aqueous suspension modified PS300 at Θ_{TMS} = 37.2% forms aggregates of 50–200 nm in size and can bind significant amounts of water (up to ~5 g/g). Only 0.5 g/g of this water is strongly bound, while the major fraction of water is weakly bound. The presence of surface TMS groups causes the appearance of weakly associated water (WAW) at the interfaces. The adsorption of methane and hydrogen onto TMS-nanosilica with pre-adsorbed water (hydration degree h = 0.05 or 0.005 g/g) increases with increasing temperature. In weakly polar $CDCl_3$ medium, interfacial water exists in strongly (SAW, chemical shift δ_H = 4–5 ppm) and weakly (δ_H = 1–2 ppm) associated states, as well as strongly (changes in the Gibbs free energy $-\Delta G$ > 0.5–0.8 kJ/mol) and weakly ($-\Delta G$ < 0.5–0.8 kJ/mol) bound states. WAW does not dissolve TFAA but some fraction of SAW bound to TMS-nanosilica surface can dissolve TFAA.

1. Introduction

Methane and hydrogen are not only important energy resources but also gases used in many industrial applications. One of the main problems of their industrial usage is very low liquefaction temperature. Therefore, research and development of inexpensive accumulator materials, able to retain large amounts of natural gases per volume unit, is of interest from a practical point of view, as well as different aspects of this problem related to interfacial phenomena [1–28]. Several methods such as chemical bonding of hydrogen, its dissolution in the volume of some matter, adsorption of methane and hydrogen by such microporous materials at high specific surface area (S_{BET}) as nanoporous activated carbons with S_{BET} > 1000 m^2/g, can be used to bind natural gases [1–8]. Disadvantages of carbons and many other adsorbents include a low rate of adsorption/desorption of hydrogen or methane in narrow pores in relatively large particles, a decrease in adsorption capacity with increasing contribution of broader transport pores (meso- or macropores), as well as a relatively low adsorption capacity of carbon adsorbents. In contrast to these adsorbents recently developed metal–organic frameworks (MOFs), possessing fantastic S_{BET} values of up to 7100 m^2/g and pore volume up to 7.55 cm^3/g [9], are characterized by very high adsorption capacity for hydrogen and methane at high pressures [9–13]. For instance, hydrogen bound to MOFs at 77 K exhibit adsorption capacities of 0.07–0.13 g/g at 60 bar, 0.2 g/g at 200 bar, and 0.2 g/g at 298 K and 500 bar [9]. For methane bound to MOFs at 298 K, adsorption capacity was 0.35 g/g at 80 bar and 1.4 g/g at 200 bar [9]. The MOFs are heterogeneous hybrid materials, and this specific chemistry of their surface can play an important role in strong binding of light gases. A relatively high adsorption of methane (up to 236 v/v) is also observed for graphenes [14]. Typically, a much lower adsorption of light gases is observed for various oxides [15–17] characterized by a smaller specific surface area than carbon or MOF materials. Results on the influence of the textural characteristics, surface chemistry, pressure and temperature on the adsorption of light gases were also obtained for polymers [18–20], hybrid adsorbents [21,22], and other materials [23,24]. Clathrate structures with hydrates of molecules of light gases (such as $CH_4 \cdot 5.75H_2O$) are also of interest [25,26]; however, they provide a smaller capacity than MOFs at similar high pressures. Water is clustered not only

* Corresponding author. Fax: +380 44 424 3567.
E-mail address: vlad_gunko@ukr.net (V.M. Gun'ko).

http://dx.doi.org/10.1016/j.jcis.2014.08.008
0021-9797/

at oxide surfaces [29] but also at the surface of activated carbons [30,31], and this can affect the adsorption of light gases. Thus, high specific surface area at predominant contribution of nanopores ($R < 1$ nm) and narrow mesopores ($R = 1–2$ nm) play an important role in enhanced adsorption of light gases. However, there are additional factors such as topography and heterogeneity of pore walls that can affect the adsorption of light gases [29]. This aspect will be analyzed in the present work.

One of the ways to enhance the adsorption of hydrogen or methane is the use of co-adsorbates and/or adsorbents with a mosaic surface (i.e., a surface of varied topography and chemical heterogeneity). Co-adsorbates can form supramolecular non-clathrate structures with target gases, or change the topology of pores (e.g., pores become narrower due to formation of co-adsorbate clusters) for more effective adsorption of the gases [29,32–40]. Previously [29,32–34] it was shown that varying amounts (dependent on adsorbent chemistry and texture) of water pre-adsorbed onto adsorbents such as activated carbons, nanosilicas, and polymer/oxide composites can enhance the adsorption of methane and hydrogen at temperatures lower than the freezing point of bulk water but higher than the freezing point of water confined in narrow pores. Complex clustered structures of co-adsorbates bound to an adsorbent surface at standard pressure differ from clathrate hydrates, which can be formed only at high pressures [25,26,41,42]. Features of clustered structures depend on the amounts and types of co-adsorbates, and textural and structural characteristics of the adsorbents. However, there are trends in the effects of co-adsorbates and/or a mosaic structure (i.e., enhanced hydrophilic/hydrophobic heterogenization of a surface with changed topography of pore walls) of an adsorbent surface [29,32–40]. Nanosilicas are generally good adsorbents for large molecules such as polymers or proteins, since the primary particles are nonporous but their aggregates are more mesoporous. These materials are also of interest for the enhanced co-adsorption of light gases (H_2 and CH_4) utilizing pre-adsorbed water, or other co-adsorbates, due to strongly clustered adsorption of polar molecules such as water, especially at a mosaic silica surface. To increase clustering of adsorbates, a partially silylated silica surface [43] can be used to prepare a mosaic surface with hydrophilic and hydrophobic patches [29,35,36]. Thus, a partial silylation of a silica surface can enhance the clusterization of adsorbed water which (i.e., ice crystallites and unfrozen clusters) changes the topography of the surface and increases a number of places appropriate for adsorption of molecules of light gases. The effect of pre-adsorbed water on subsequent adsorption of light gases can be nonlinear vs. water content [29].

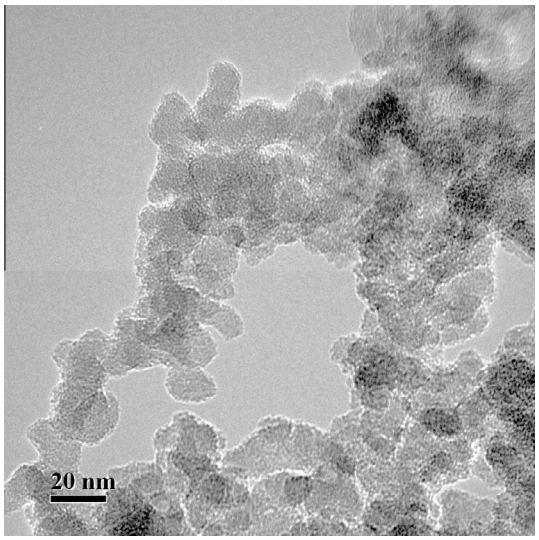

Fig. 1. High-resolution TEM (JEM-2100F, Japan) image of initial nanosilica PS300 showing aggregates of primary nanoparticles.

Fumed silicas (nanosilicas at $S_{BET} = 50–500$ m^2/g) are hydrophilic adsorbents which can bind large amounts of water in aqueous suspensions [29]. However, nanosilicas in the powdered state bind small amounts of water (2–5 wt.%) adsorbed from air at room temperature and RH ≈ 70–80%. Dry unmodified nanosilicas possess low adsorption ability with respect to light gases [29]. To increase adsorption capacity by increasing adsorbate clustering, nanosilica can be partially modified, e.g., hydrophobized by trimethylsilyl (TMS) groups. In general, modification should not be very high (because the adsorption potential of a modified surface is reduced) or very low (because enhanced adsorbate clustering will not occur). Therefore, 37.2% substitution of silanols by TMS groups at the PS300 surface was selected to study the enhanced adsorption of light gases. In addition the effects of different dispersion media on the interfacial behavior of water and co-adsorbates were studied. Notice that the present study was rather devoted to the interfacial phenomena related to co-adsorption of light gases and water than to the synthesis of materials possessing very high adsorption capacity (such as MOFs) for light gases.

2. Materials and methods

2.1. Materials

Pyrogenic (fumed) silica PS300 (pilot plant of the Chuiko Institute of Surface Chemistry, Kalush, Ukraine) with $S_{BET} = 320$ m^2/g and 0.8 mmol/g of free silanols was used as the starting material. Partially silylated nanosilicas were produced using trimethylethoxysilane $(CH_3)_3SiOC_2H_5$ as a modifier at the substitution degree of surface silanols of 27.2% (sample HS1) and 37.2% (sample HS2). The modification reaction was performed at 150–160 °C for 3 h in a glass reactor with a mixer (300–500 rpm) with addition of acetic acid (0.144 g per gram of dry silica) as a catalyst. After the reaction, modified silica was heated in an oven at 300 °C for 2 h to remove residual silane, acetic acid and side products.

The amounts of free surface silanols and attached trimethylsilyl (TMS) groups were estimated by infrared (IR) spectroscopy using a Specord M80 (Carl Zeiss, Jena) spectrophotometer. The modification degree of the silica surface by the TMS groups (Θ_{TMS}, %) was estimated from the ratio of optical density of a band of free silanols at 3750 cm^{-1} of modified and unmodified silicas (spectra recorded in the 4000–1200 cm^{-1} range using thin pellets with silica samples)

$$\Theta_{TMS} = 100\left(1 - \frac{D}{D_0}\right), \quad (1)$$

where D_0 and D are the optical density of the mentioned band of the unmodified and modified silicas, respectively. Notice that this approach gives the TMS group content close to that estimated using thermogravimetry or element analysis methods [29,33–36]. Additionally, the IR spectra in the range of 2000–300 cm^{-1} were recorded using a blend of samples with dry KBr (1:400).

The hydrophilicity coefficient (β) of samples was as the ratio the heats of immersion in water (Q_w) and *n*-decane (Q_d)

$$\beta = \frac{Q_w}{Q_d}. \quad (2)$$

A microcalorimetric study of nanosilicas was carried out with a DAC1.1A (EPSE, Chernogolovka) differential automatic calorimeter calibrated using the known heat effect of dissolution of KCl in water (18.6 ± 0.012 kJ/mol at 20 °C). Before the heat of immersion measurements in water or decane, silica samples (50 mg) were

degassed at 473 K and 0.01 Pa for 2 h and then used without air contact. The amount of sample used was 50 mg per 3 ml of distilled water or decane. The Q values were measured during exposure of the mixture for several hours. The average errors of the Q measurements repeated several times were smaller than ±10%.

2.2. ^{1}H NMR spectroscopy

^{1}H NMR spectra of static samples of nanosilicas with different adsorbates were recorded using a Varian 400 Mercury spectrometer (magnetic field 9.4 T) utilizing 90° pulses of 3 μs duration. Each spectrum was recorded by co-addition of eight scans with a 2 s delay between each scan. Relative mean errors were less than ±10% for ^{1}H NMR signal intensity for overlapped signals, and ±5% for single signals. Temperature control was accurate and precise to within ±1 K. The accuracy of integral intensities was improved by compensating for phase distortion and zero line nonlinearity with the same intensity scale at different temperatures. To prevent supercooling, spectra were recorded at T = 210 K (for samples precooled to this temperature for 10 min), then heated to 280 K at a rate of 5 K/min with steps ΔT = 10 K or 5 K (with a heating rate of 5 K/min for 2 min), and maintained at a fixed temperature for 8 min for data acquisition at each temperature. Applications of this method and NMR cryoporometry to nanooxides were described in detail elsewhere [29,32–40]. Changes in the Gibbs free energy (ΔG) of bound water and free surface energy (γ_S), as the modulus of integrated changes of the ΔG values in the bound water layers, were determined from the temperature dependences of the amounts of unfrozen water (C_{uw} in mg of water per gram of dry silica) at T = 210–273 K [29] and tabulated ΔG data for ice [44]. The average melting temperature $\langle T\rangle$ was calculated using formula [29]

$$\langle T\rangle = \int_{T_{min}}^{T_0} TC_{uw}(T)dT \Big/ \int_{T_{min}}^{T_0} C_{uw}(T)dT, \quad (3)$$

where T_0 = 273.15 K, and T_{min} is the temperature corresponding to C_{uw} = 0.

Water can be frozen in narrower pores at lower temperatures as described by the Gibbs–Thomson relation for the freezing point depression for liquids confined in cylindrical pores at radius R [29,45–47]

$$\Delta T_m = T_{m,\infty} - T_m(R) = -\frac{2\sigma_{sl}T_{m,\infty}}{\Delta H_f \rho R} = \frac{k_{GT}}{R}, \quad (4)$$

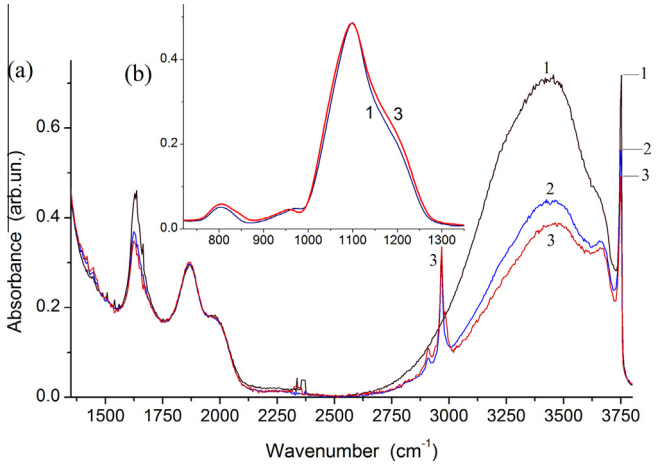

Fig. 2. IR spectra of PS300 unmodified (curve 1) and modified at Θ_{TMS} = 27.2% (2) and 37.2% (3); the spectra of modified silicas were normalized to the intensity of the band at (a) 1867 cm^{-1} or (b) 1100 cm^{-1} of unmodified silica.

Table 1
Heat of immersion of unmodified and modified silicas in water and n-decane.

Θ (%)	Q_w (J/g)	Q_d (J/g)	$\beta = Q_w/Q_d$
0	48	22.0	2.0
27.2	39	24.5	1.6
37.2	33	24.0	1.4

where $T_m(R)$ is the melting temperature of ice in cylindrical pores of radius R, $T_{m,\infty}$ the bulk melting temperature, ΔH_f the bulk enthalpy of fusion, ρ the density of the solid, σ_{sl} the energy of solid–liquid interaction, and k_{GT} is the Gibbs–Thomson constant (here 50 K nm). Eq. (4) was used to determine the distribution function ($f_V(R) = dV_{uw}(R)/dR$) of sizes of water structures unfrozen at T < 273 K [29] and adsorbed onto silicas.

Samples were prepared using 50 mg of silica (hydration degree h = 0.05 g/g) placed into a 5 mm ampoule connected to a rubber vessel with methane (2 L, 1.1 bar). Additional portions of methane can be adsorbed onto a sample during NMR measurements with decreasing temperature. Similar measurements were carried out for hydrogen but at smaller h = 0.005 g/g.

Silica (0.3 g) was stirred with 0.3 g of water to form a uniform system which was then dried at 400 K for 15 min. This compacted powder was more dense (~0.25 g/cm^3) by a factor of approximately five than the initial silica powder. A more strongly hydrated silica sample was prepared by mixing 200 mg of silica with 240 mg of water (dilute suspension), or addition of 2.6 g of water to 0.2 g of silica (concentrated suspension).

2.3. Aqueous suspensions

Particle size distributions and electrophoretic mobility of particles (re-calculated to the ζ potential [48]) of unmodified and modified nanosilicas were measured (at 298 K) for dilute aqueous suspensions (0.02 wt.%) using a Zetasizer 3000 (Malvern Instruments) apparatus based on the photon correlation spectroscopy (PCS), (laser wavelength λ = 633 nm, scattering angle Θ = 90°). The highly diluted suspensions sonicated for 5 min using an ultrasonic disperser (Sonicator Misonix Inc.) (22 kHz and 500 W) were used to reduce particle–particle interactions. To compute the particle size distribution (PaSD) with respect to the intensity of light scattering ($PaSD_I$) and particle volume ($PaSD_V$) and number ($PaSD_N$), the Malvern Instruments software was utilized, assuming that particles had a roughly spherical shape.

According to the Smoluchowski theory [48], there is a linear relationship between the electrophoretic mobility U_e and the ζ potential: $U_e = A\zeta$, where A is a constant for a thin electrical double layer (EDL) at $\kappa a \gg 1$ (where a denotes the particle radius, and κ is the Debye–Huckel parameter). For a thick EDL (κa < 1), e.g., at pH close to the isoelectric point (IEP), the equation with the Henry correction factor is more appropriate $U_e = 2\varepsilon\,\zeta/(3\eta)$, where ε is the dielectric permittivity; and η is the viscosity of the liquid. The pH values were adjusted by addition of 0.1 M HCl or NaOH solutions.

2.4. Quantum chemical calculations

Quantum chemical calculations were carried out using *ab initio* and DFT methods (functionals B3LYP and wB97XD (better describing dispersion interactions) with the 6-31G(d,p) basis set) using the Gaussian 09 [49] program suite, to full geometry optimization of molecules or clusters. The δ_H values were calculated as the difference in the isotropic values of the magnetic shielding tensors of H atoms ($\sigma_{H,iso}$) of tetramethylsilane, TeMS ($\delta_{H,TeMS}$ = 0 ppm) as a reference compound ($\sigma_{H,iso}$ = 31.76, 32.03, and 31.77 ppm for

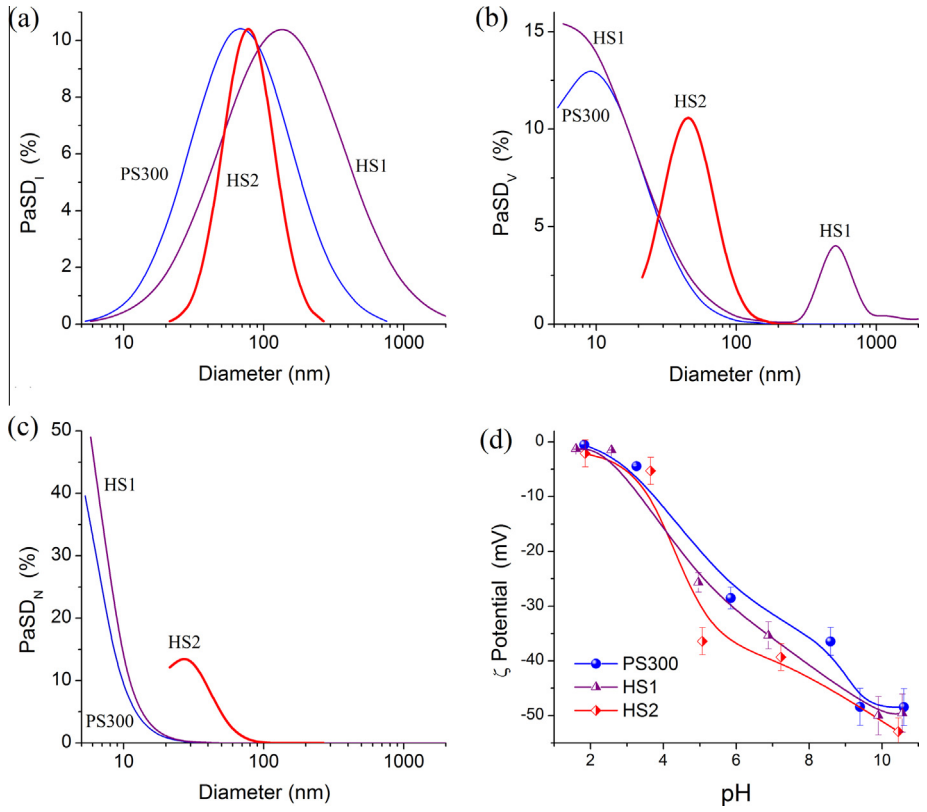

Fig. 3. Particle size distributions with respect to (a) scattered light intensity, (b) particle volume, (c) particle numbers, and (d) zeta-potentials of PS300, HS1, and HS2 samples in the diluted (0.02 wt.%) aqueous suspensions.

TeMS by GIAO with B3LYP/6-31G(d,p)//HF/6-31G(d,p), wB97XD/6-31G(d,p)//HF/6-31G(d,p), and wB97XD/6-31G(d,p), where HF/6-31G(d,p) was used for the geometry optimization) and a given compound. The gauge-independent atomic orbital (GIAO) method [49] with B3LYP/6-31G(d,p) or wB97XD/6-31G(d,p) was used for relatively small systems (<200 atoms). Large structures (up to 6000 atoms) were calculated using the PM7 method (MOPAC 2012 package) [50,51]. To calculate the $f(\delta_H)$ functions using the PM7 results, a calibration function was used to describe the dependence between atomic charges q_H (PM7) and the δ_H values (GIAO/B3LYP/6-31G(d,p)) calculated for relatively small systems. Visualization of structures with hydrated unmodified and modified silica nanoparticle was carried out using UCSF Chimera (version 1.9, May 2014) [52] or ChemCraft [53] or Jmol [54].

3. Results and discussions

3.1. Structural features of unmodified and silylated silicas

Initial fumed silica studied is composed of nonporous nanoparticles (average diameter $d_{av} = 6/(\rho_0 S_{BET}) \approx 8.5$ nm (size distribution mainly 5–18 nm [29]) with a true density of amorphous nanosilica $\rho_0 = 2.2$ g/cm^3) forming aggregates (Fig. 1) and agglomerates of aggregates. Voids between primary nanoparticles in the secondary structures are responsible for the textural porosity of the silica powders [29,55–57]. Silylation of the silica surface to form a mosaic coverage with TMS groups marginally affects the particulate morphology; however, the nanoparticle size increases slightly since the specific surface area decreases after silylation [29]. Wetting or suspending and drying of nanosilicas affect the organization of secondary particles that lead to an increase in the bulk density from 0.04–0.06 g/cm^3 to 0.25–0.30 g/cm^3. This is also accompanied by enhancement of mesoporosity of nanosilicas; i.e., the contribution of pores at radius 1 nm < R < 25 nm to the total porosity increases. However, contributions of nanopores and macropores can decrease due to compaction of silica nanoparticles in aggregates. These textural features can influence the interfacial behavior of water, methane and hydrogen.

Typically, hydrophobicity of silica increases with increasing TMS content on the surface [29,35]. A similar result is observed for silicas studied here (Fig. 2, Table 1). A decrease in hydrophilicity (accompanied by an increase in intensity of the C—H stretching vibration bands of the TMS groups at 2970 and 2907 cm^{-1}) of modified silicas is accompanied by a decrease in the adsorption of water from air. This leads to a reduction of intensity of the broad band of adsorbed water at 3300 cm^{-1} (Fig. 2a). Deconvolution of a broad band of the O—H stretching vibrations (into four bands for PS300 and six bands for HS1 and HS2 due to the presence of two C—H bands [29]) gives integral intensity of a band of strongly bound water or strongly disturbed silanols at 3290–3280 cm^{-1} as 68.2%, 56.0%, and 50.8% for PS300, HS1, and HS2, respectively. Relative contribution of slightly disturbed silanols at 3670–3680 cm^{-1} (which are poorly accessible for adsorbates) increases for modified silicas, since integral intensity of this band is 5.2%, 7.8%, and 8.1% for PS300, HS1, and HS2, respectively.

Notice that there is a slight broadening of a band of asymmetric Si–O stretching vibrations at 1150–1250 cm^{-1} of HS2 in comparison with PS300 (Fig. 2b). This can be due to surface ≡Si—O—Si(CH$_3$)$_3$ groups (the spectra were normalized to the intensity of the band at (Fig. 2a) 1867 cm^{-1} (which is the bulk silica overtone mode proportional to the total mass of silica probed by the IR beam and used as the inner standard) or (Fig. 2b) 1100 cm^{-1} (Si—O stretching vibrations) of unmodified silica). Typ-

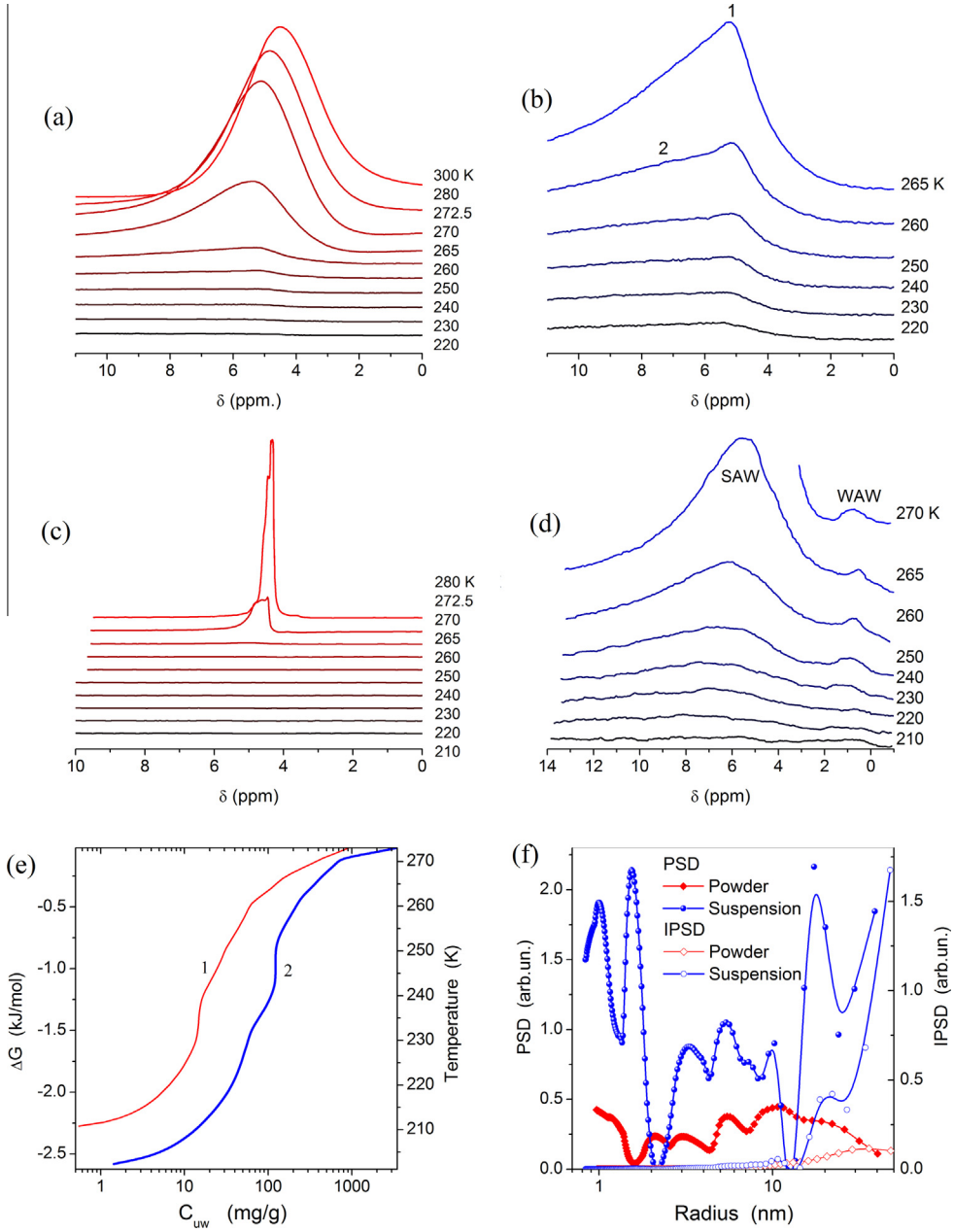

Fig. 4. ^{1}H NMR spectra recorded at different temperatures of water bound to modified PS300 (HS2, Θ = 37.2%) for (a and b) wetted powder at h = 1.2 g/g and (c and d) aqueous suspension at h = 13 g/g, (e) amounts of unfrozen water C_{uw} vs. temperature and vs. changes in the Gibbs free energy of bound water (errors < ±10%), and (f) size distributions of unfrozen water clusters bound to silica in wetted powder and aqueous suspension (figures b and d correspond to subsets of figures a and c at low temperatures).

ically, a decrease in separation between the cooperative Si—O—Si asymmetric modes at 1100 cm^{-1} (i.e., band narrowing) in the IR spectra of silica is usually associated with an increase in the polymerization degree, i.e., an increase in the number of Si—O—Si bonds in larger particles [55–58]. However, it is difficult to suppose that silica nanoparticles' size decreases during silylation since the specific surface area of modified silica decreases. Therefore, the observed broadening (Fig. 2b) could be assigned to the surface groups because their symmetric and asymmetric stretching vibrations can occur at higher frequency.

Calculations of the specific surface area according to the IR data [59] (using the normalized ratio of integral intensity of the bands at 1867 and 3750 cm^{-1}) give S_{IR} = 328, 296, and 250 m^2/g at Θ_{TMS} = 0 (PS300), 27.2% (HS1), and 37.2% (HS2), respectively. This reduction of the S_{IR} value can be due to two effects. First, real diminution of the specific surface area is due to attaching TMS groups. Second, diminution of the content surface silanols causes apparent decrease in the specific surface area since this content is used to estimate the S_{IR} value [59]. Thus, real diminution of the specific surface area is slightly smaller than the S_{IR} value shows [29]. The reduction of the specific surface area of modified silica with increasing modification degree was observed previously [29,35,60]. Besides this surface area reduction, the adsorption potential also decreases with increasing Θ value with respect to both polar and nonpolar compounds and polymers [29]. Thus, the interfacial behavior of such co-adsorbates as methane or hydrogen and water can depend on several factors: (i) the textural characteristics vs. surface composition; (ii) changes in the adsorp-

Table 2
Characteristics of unfrozen water bound to modified silica (HS2, Θ = 37.2%) at different conditions.

Sample	h (g/g)	V_{uw} (cm^3/g)	S_{uw} (m^2/g)	$S_{uw,nano}$ (m^2/g)	$S_{uw,meso}$ (m^2/g)	$S_{uw,macro}$ (m^2/g)	$V_{uw,nano}$ (cm^3/g)	$V_{uw,meso}$ (cm^3/g)	$V_{uw,macro}$ (cm^3/g)	γ_S (J/g)	$\langle T\rangle$ (K)	$-\Delta G_s$ (kJ/mol)
Wetted powder	1.2	0.965	62	3	52	7	0.001	0.860	0.103	9.91 ± 1.0	267.45	2.31 ± 0.2
Suspension	13	4.325	287	47	143	97	0.022	2.628	1.675	34.86 ± 3.5	267.96	2.62 ± 0.3
Weakly wetted powder + CH_4	0.05	0.050	15	12	3	0	0.005	0.045	0	3.36 ± 0.34	230.92	2.63 ± 0.3
Nearly dry powder + H_2	0.005	0.005	0.3	0	0.3	0	0	0.005	0	0.12 ± 0.01	258.33	1.63 ± 0.2
Powder in $CDCl_3$ + TFAA	0.05	0.038	19	15	4	0	0.007	0.031	0	2.49 ± 0.25	242.27	2.63 ± 0.3

Note: V_{uw} is the volume of bound water unfrozen at T < 273 K; S_{uw} is the specific area of silica in contact with unfrozen water; nano-, meso- and macro-components of S_{uw} and V_{uw} are determined by integration of the distribution functions at radius values of 0.3–1.0 nm (nano), 1–25 nm (meso), and 25–100 nm (macro); γ_S is the surface free energy (in J per gram of dry oxide); $\langle T\rangle$ is the average melting temperature; and ΔG_s is changes in the Gibbs free energy of strongly bound water.

tion potential; (iii) changes in clustered adsorption of water; (iv) freezing and melting points of co-adsorbates; (v) current temperature, and (vi) concentration of co-adsorbates and dispersion medium type. Here some of these aspects are analyzed with low-temperature ^{1}H NMR measurements.

Partial silylation of PS300 (Θ_{TMS} = 27.2% and 37.2%) causes an increase in nanoparticle aggregation observed in the suspension with increasing Θ_{TMS} value (Fig. 3a–c). This can be explained by rearrangement of modified silica nanoparticles in aggregates to reduce the contact area between hydrophobic TMS groups and water molecules. Notice that the aggregation is higher for HS1 than for HS2. This can be explained by a greater nonuniformity of the surface at a lower degree of the silylation. Similar effects were observed previously [29].

However, the observed changes in aggregation are similar to typical changes in aggregation of different unmodified nanosilicas [61]; i.e., they are not extensive since the silica surface is only partially hydrophobized. Additionally, changes in the zeta-potential of partially modified nanosilicas are relatively small compared to the initial silica (Fig. 3d). Notice that only a portion of surface silanols is deproponated in the used range of pH. In other words, the modified silica surface has enough number of silanols to provide a close value of the surface charges. Additionally, the zeta-potential is linked to average charging under slipping plane in the electrical double layer (EDL) around primary particles and their aggregates. Thus, partial silylation of the nanosilica surface leads also to changes in a dense part of EDL.

For modified nanosilicas in more concentrated aqueous suspensions, stronger aggregation can be expected than observed here for the more diluted suspensions or for unmodified silicas [29,61]. Therefore, one can expect that the aggregation of modified silica nanoparticles can affect the interfacial behavior of water bound to a surface.

3.2. Interaction of water with modified silica

Water adsorbed onto a surface of any adsorbent can exist in clusters due to nonuniformity of the surface (e.g., mosaic coverage with surface hydroxyls) if the water amounts are relatively small (<20 wt.% for nanosilica [29]). Additionally, bulk or bound water tends to form a maximum number of hydrogen bonds per molecule possible [29,62]. The appearance of hydrophobic TMS groups at a silica surface (with mosaic ≡Si—OH and ≡Si—O—Si$(CH_3)_3$ coverage) can affect the structure of bound water (Fig. 4). At a relatively high hydration degree h = 1.2 g/g, water can form a continuous layer at the modified silica (HS2) surface. Therefore, the only signal observed is from strongly associated water (SAW) [29] in the ^{1}H NMR spectra (mobile at T < 273 K), identified by the chemical shift of the proton resonance δ_H = 5.0–5.5 ppm (Fig. 4a). These δ_H values are typical for hydrated silicas [29,63] and close to that of bulk liquid water. At 265 K < T < 273 K, a main fraction of this water is frozen. Therefore, it can be assigned to weakly bound water (WBW) [29]. At low temperatures, two relatively weak signals are observed at 5 ppm (signal 1) and 7 ppm (signal 2) (Fig. 4b). On the basis of freezing temperatures and δ_H values, this water can be assigned to strongly bound water (SBW) [29] of the SAW type. The δ_H value of signal 2 is close to that of ice. This ordering of interfacial water (similar to ice) can be caused by the effects of hydrophobic TMS groups on the water [29,62].

In the concentrated aqueous suspension at h = 13 g/g, besides the signal of SAW at δ_H = 4.5–6.0 ppm (Fig. 4c and d), a signal of weakly associated water (WAW) is also observed at $\delta_H \approx 1$ ppm. This can be explained by water filling of adsorption sites at the surface in a confined space between neighboring TMS groups.

In the case of wetted powder (h = 1.2 g/g), the degree of filling of these sites by water is likely much lower (i.e., the hydration shells of nanoparticles are nonuniform) than in the suspension. WAW corresponds to 1D, 2D or branched 3D clusters, in which a relative number of the H atoms in the hydrogen bonds are smaller than 50% [27]. The complex signal shape seen at 272.5 K and 280 K (Fig. 4c) may be due to nonuniformity of the modified silica.

Typically for wetted powders, the greater the adsorbed water amount, the smaller the fraction of strongly bound water. In other words, the WBW fraction increases with increasing water content because the amount of water distant from the adsorbent surface increases. In the case of an aqueous suspension, three main types of water can be present: SBW, WBW and bulk (unbound water, UW) water, and one can expect that all of the water is SAW. There are two sections in the $C_{uw}(T)$ curves (Fig. 4e) corresponding to SBW (at lower Gibbs free energy, ΔG) and WBW (at higher Gibbs free energy). The amounts of SBW are 0.13 and 0.45 g/g for the wetted powder and the suspension, respectively, while the total volume of bound water is 0.965 and 4.325 cm^3/g, respectively (Table 2, V_{uw}). Contact area between bound water and the HS2 surface increases nearly fivefold in the suspension (Table 2, S_{uw}). Therefore, contributions of structures of three types of water-filled nanopores (at radius R < 1 nm, $S_{uw,nano}$, $V_{uw,nano}$), mesopores (1 nm < R < 25 nm, $S_{uw,meso}$, $V_{uw,meso}$) and macropores (25 nm < R < 100 nm, $S_{uw,macro}$, $V_{uw,macro}$) all increase significantly. Changes in contacts between bound water and the HS2 surface cause an increase in the interaction energy. Therefore, the surface energy increases by several times (Table 2, γ_S), and the Gibbs free energy of the first adsorption layer (corresponding to SBW) decreases (ΔG_s). It should be noted that the γ_S values are calculated in J per gram of dry silica. Therefore, at a small content of adsorbed water these values are small (Table 2, h = 0.05 or 0.005 g/g). However, in the case of wetted powder, the γ_S value is small despite h = 1.2 g/g that suggests weak interactions between water and HS2.

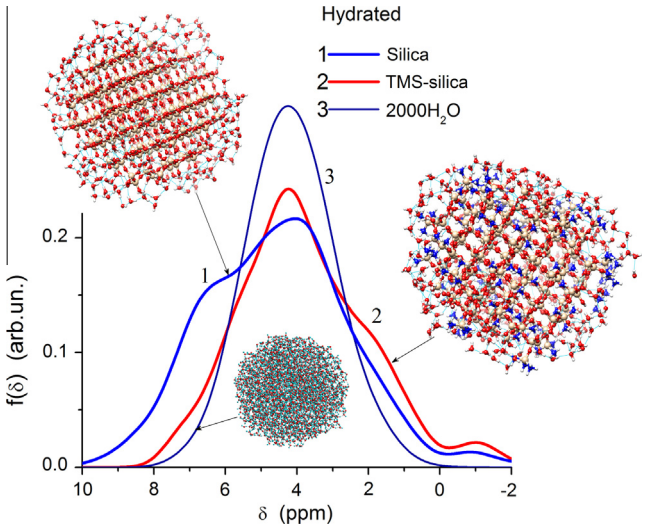

Fig. 5. Theoretically calculated ^{1}H NMR spectra (by PM7) of water ($\sim$200H_2O) bound to unmodified (curve 1, 828 atoms) or partially modified (curve 2, 1272 atoms) silica particle, and pure water with 2000H_2O (curve 3).

The average melting temperature for water bound in the suspension is close to that for the wetted powder (Table 2, $\langle T \rangle$). The $\langle T \rangle$ values for wetted powder and concentrated suspension suggest that WBW is predominant in both systems, in agreement with the dependences of C_{uw} vs. ΔG and T (Fig. 4e) showing that the major portion of bound water is WBW. This is also in agreement with the bound water cluster sizes (Fig. 4f), since water in larger clusters should be more weakly bound to the surface as their distance from the surface increases. There is a tendency of a decrease in the $\langle T \rangle$ value with decreasing hydration degree (Table 2). However, this also depends on other conditions (e.g., compare systems at h = 0.05 and 0.005 g/g, Table 2).

According to theoretically calculated ^{1}H NMR spectra, water bound to nanosilica is characterized by a broader band exhibiting a larger contribution of water with downfield shift (Fig. 5, curve 1) in comparison with pure water (curve 3). Water (SAW) bound to silylated silica surface is characterized by an upfield shift with appearance of WAW at 1–2 ppm (Fig. 5, comp. curves 2 and 1) similar to experimentally observed spectra. These effects are due to enhanced clustering of water bound to TMS-silica with mosaic hydrophilic–hydrophobic patches, in comparison with water bound to an unmodified silica surface.

3.3. Co-adsorption of water and methane on partially silylated nanosilica

Methane molecules interacting with adsorbents due to weak van-der-Waals bonds can be effectively adsorbed only into nanopores or narrow mesopores. Therefore methane adsorption onto nanosilica is relatively low, particularly on unmodified nanosilicas [29,33]. It was also shown that co-adsorbed water can increase the adsorption of methane. To increase methane adsorption, partially silylated nanosilica HS2 is used here with a small amount of preadsorbed water (h = 0.05 g/g). This water, partially freezing at T < 273 K, can change the topography of the silica surface and the topology of voids between adjacent nanoparticles. Under these conditions, clathrate formation is impossible (clathrates only form at high pressures) and the low content of water forming strongly clustered structures at residual silanols located between attached TMS groups.

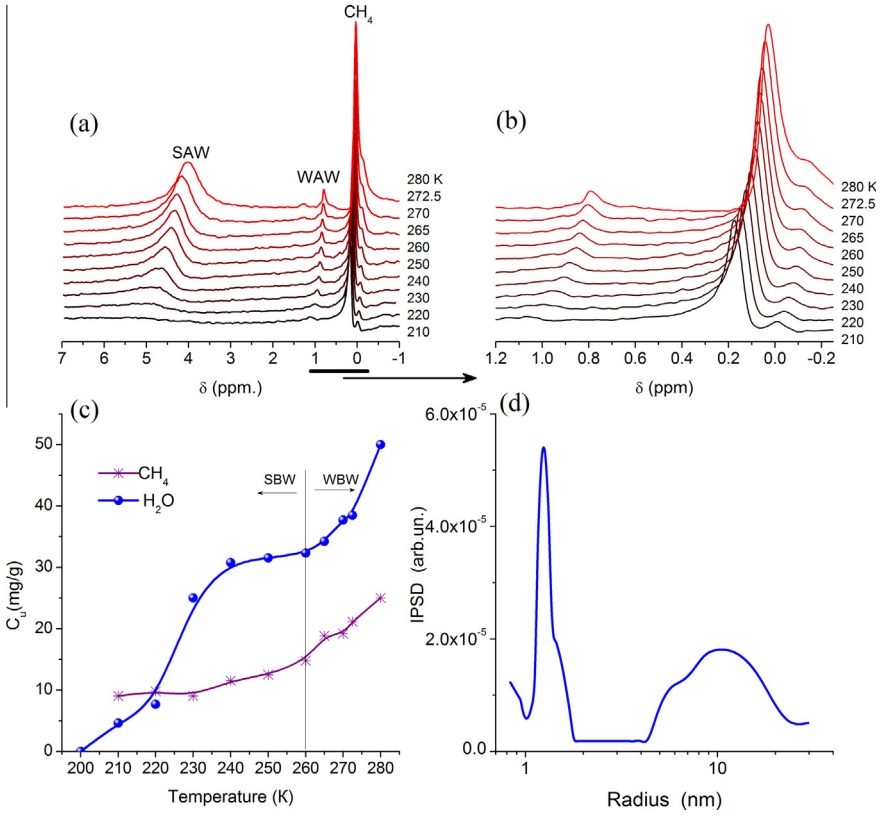

Fig. 6. (a and b) ^{1}H NMR spectra recorded at different temperatures of water and methane bound to HS2, (c) temperature dependences of concentrations bound unfrozen water and adsorbed methane (errors < ±10%), and (d) size distribution of voids filled by unfrozen water.

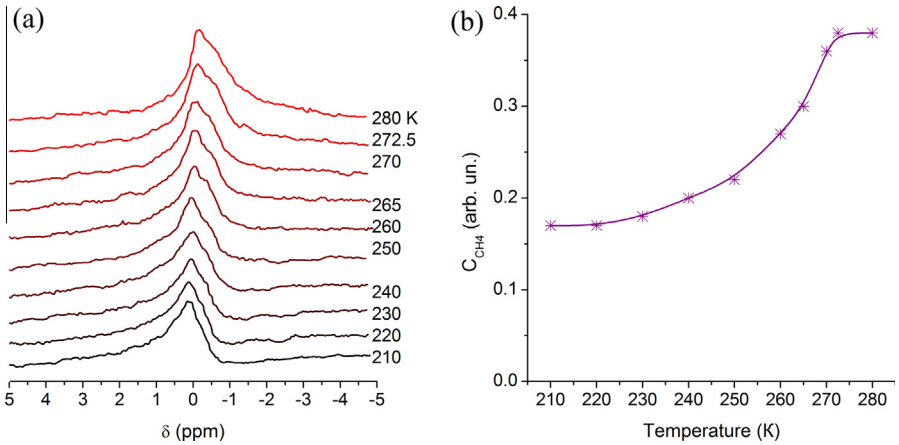

Fig. 7. (a) ^{1}H NMR spectra recorded at different temperatures of water (h = 0.005 g/g) and methane bound to compacted HS2 and (b) changes in the methane adsorption with temperature (errors < ±10%).

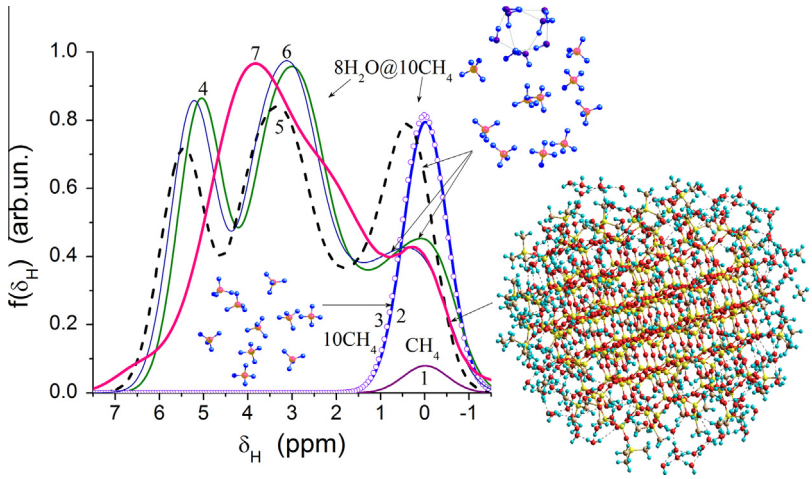

Fig. 8. ^{1}H NMR spectra of water and methane in different structures: CH_4 (curve 1), $10CH_4$ (2 and 3), and $10CH_4@8H_2O$ (curves 4–6) calculated with GIAO using B3LYP/6-31G(d,p)//HF6-31G(d,p) (curves 1, 2 (line), and 4) wB97XD//HF6-31G(d,p) (curve 5) or wB97XD (curve 6), and PM7 with a correlation function ($10CH_4$, 3 (symbols) and water molecules bound to TMS-silica nanoparticle with co-adsorbed methane molecules, curve 7).

HS2 with pre-adsorbed water (h = 0.05 g/g leads to a larger content of SAW than WAW or SBW than WBW), various portions of which can be frozen at different temperatures, is a nonuniform adsorbent for methane (Fig. 6).

This nonuniformity is also observed in the distribution of unfrozen water structures filling voids between silica particles (Fig. 6d) and structural characteristics of voids filled by bound water (Table 2). Therefore, two signals of methane are observed in the ^{1}H NMR spectra at δ_H = −0.1–0.4 ppm (Fig. 6a and b). Signal intensity of methane increases with increasing temperature (Fig. 6a). The amounts of unfrozen water and adsorbed methane vs. temperature (Fig. 6c) demonstrate concerted changes at T > 240 K. This can be caused by changes in the topology of voids (pores) where melting of water occurs resulting in increased mobility of water molecules with increasing temperature. The observed downfield shift of methane signal with lowering temperature can be caused by the temperature dependence of the sample's magnetic susceptibility [64]. In the case of weakly hydrated unmodified nanosilica (h = 0.005 g/g), methane adsorption decreases from 0.034 g/g at 200 K to 0.01 g/g at 280 K, opposite to the trend seen with the partially silylated nanosilica. With more highly hydrated unmodified nanosilicas when h = 0.045–0.15 g/g, methane adsorption is much lower (0.001–0.002 g/g) over this temperature range, again exhibiting decreasing adsorption with increasing temperature [33]. Thus, partial silylation of nanosilica causes changes in the adsorption trend of methane with temperature (studied here) in comparison with the unmodified silica previously studied [33]. Water is adsorbed as SAW (4–5 ppm) and WAW (0.8–1.5 ppm) (Fig. 6a). The downfield shift is observed for both water types, and this shift is stronger for SAW possessing larger sizes. This occurs due to ordering of water clusters on freezing (e.g., mobile water → amorphous ice → crystalline ice). Signal intensity decreases with lowering temperature due to water fraction freezing.

To study changes of confined space effects, additional water was added to the HS2 sample to form a wetted powder ($h \approx 1$ g/g), then stirred and heated at 400 K for 10 min (bulk density ~0.3 g/cm^3). The resulting sample contains a residual amount of bound water (h = 0.005 g/g). This water gives a broad ^{1}H NMR signal whose intensity cannot be determined (Fig. 7a); therefore, the amount of adsorbed methane is given in arbitrary units (Fig. 7b). Estimation of the CH_4 signal noise level in the spectra of initial HS2 (Fig. 6a) compared to the additionally treated HS2 (Fig. 7a), suggests that the adsorption of methane onto treated HS2 is lower than on initial HS2. This may be a result of changes in the confined space effects and the amounts of co-adsorbed water located in nar-

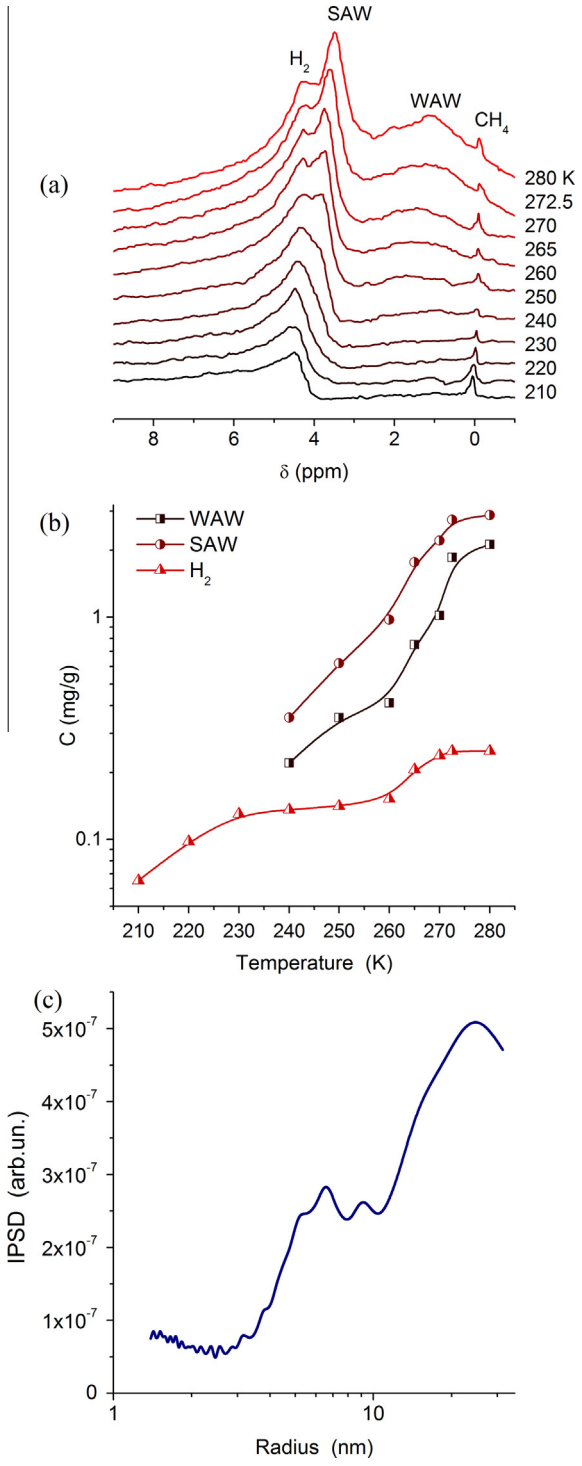

Fig. 9. (a) ^{1}H NMR spectra recorded at different temperatures of water (h = 0.005 g/g), hydrogen and methane bound to HS2, (b) amounts of WAW, SAW and hydrogen vs. temperature (average errors are smaller than ±10%), and (c) size distribution of pores filled by unfrozen water bound to HS2.

row pores most able to bind adsorbed methane molecules. However, for the treated HS2, there is a larger temperature dependence of the adsorbed amount of methane than that for the initial HS2. This result can be caused by enhancement of confined space effects in compacted nanosilica.

Theoretically calculated ^{1}H NMR spectra of water and methane in different structures (Fig. 8) show that for the H atoms of methane molecules interacting with neighboring water molecules in $10CH_4@8H_2O$ (curves 4–6), there is a downfield shift of ~1 ppm. This leads to a broadening of the methane band at 0–1 ppm (curves 4–6). The peaks at 3 and 5.5 ppm are linked to the water molecules from the same clusters. This splitting results from calculation features of clusters of restricted sizes, since experimentally there should be only one band due to fast molecular exchange. Changes in the DFT functionals (in GIAO calculations) and optimization type (DFT or HF) result in small differences in the spectra. Use of the PM7 method with the calibration function gives the spectrum of $10CH_4$ (Fig. 8, curve 3), which is close to that calculated using GIAO/B3LYP/6-31G(d,p)//HF/6-31G(d,p) (curve 2). Therefore, this approach was applied to a large system (Fig. 8, curve 7). A downfield shift for methane bound to hydrated TMS-silica nanoparticles is similar to that for $10CH_4@8H_2O$. WAW appears as a shoulder at 1–2 ppm (curve 7). SAW peak of maximum intensity is at 4 ppm, similar to the experimental data (Fig. 6a). Additionally, there is a shoulder at 6–7 ppm (Fig. 8, curve 7) similar to the experimental signal seen at low temperatures (Fig. 4b). These theoretical results confirm our interpretation of the experimental ^{1}H NMR spectra described above.

3.4. Co-adsorption of water and hydrogen on partially silylated nanosilica

Hydrogen is poorly adsorbed onto any adsorbent at normal pressure because of very weak van-der-Waals interactions. Nearly dry HS2 at h = 0.005 g/g was used here to study the interfacial behavior of hydrogen co-adsorbed with a small amount of pre-adsorbed water. Adsorbed hydrogen is observed in the low-temperature ^{1}H NMR spectra as a broadened signal at δ_H = 4.5 ppm (Fig. 9a). This broadening suggests adsorption, since the resonance for H_2 gas would be much narrower at 4 ppm. The small upfield shift for adsorbed hydrogen is due to location of the electron density in the H_2 molecules mainly between the two protons.

This leads to a decrease in their magnetic shielding upon hydrogen adsorption. Residual water is observed as both SAW at δ_H = 4.0–4.5 ppm and WAW at δ_H = 1.0–1.5 ppm (Fig. 9a). Water is in a strongly clustered state, since its contact area with the HS2 surface is very small (Table 2, S). Additionally, there is a methane signal (added to hydrogen as a standard) at δ_H = 0 ppm. In contrast to hydrogen, water is frozen with lowering temperature that leads to signal reduction at T < 260 K and its disappearance at $T \leqslant$ 220 K.

The adsorption of hydrogen onto HS2 is very low ($\leqslant$0.2 mg/g) and smaller by an order of magnitude than that of methane. Hydrogen adsorption (Fig. 9b) increases with increasing temperature, similar to the behavior of adsorbed methane (Figs. 6 and 7). Notice that despite the low content of pre-adsorbed water (Table 2), it forms both smaller (~1–2 nm) and larger (10–30 nm) structures (Fig. 9c). This corresponds to known clustered adsorption of water [29] enhanced here by partial silylation of the silica surface. Melting of ice nanocrystallites located in nanopores and narrow mesopores with increasing temperature, and enhanced mobility of water molecules, can free up a portion of these smaller pores. Such pores are better able to adsorb hydrogen molecules than larger mesopores. Therefore, the adsorption of hydrogen increases with temperature.

3.5. Effects of media on bound water

Nonpolar or weakly polar media can slow down molecular exchange between water molecules from different clusters and domains located at an adsorbent's surface. This can result in narrowing or even splitting of bands in the ^{1}H NMR spectra [29]. Addition of acids to the dispersion media allows one to differentiate

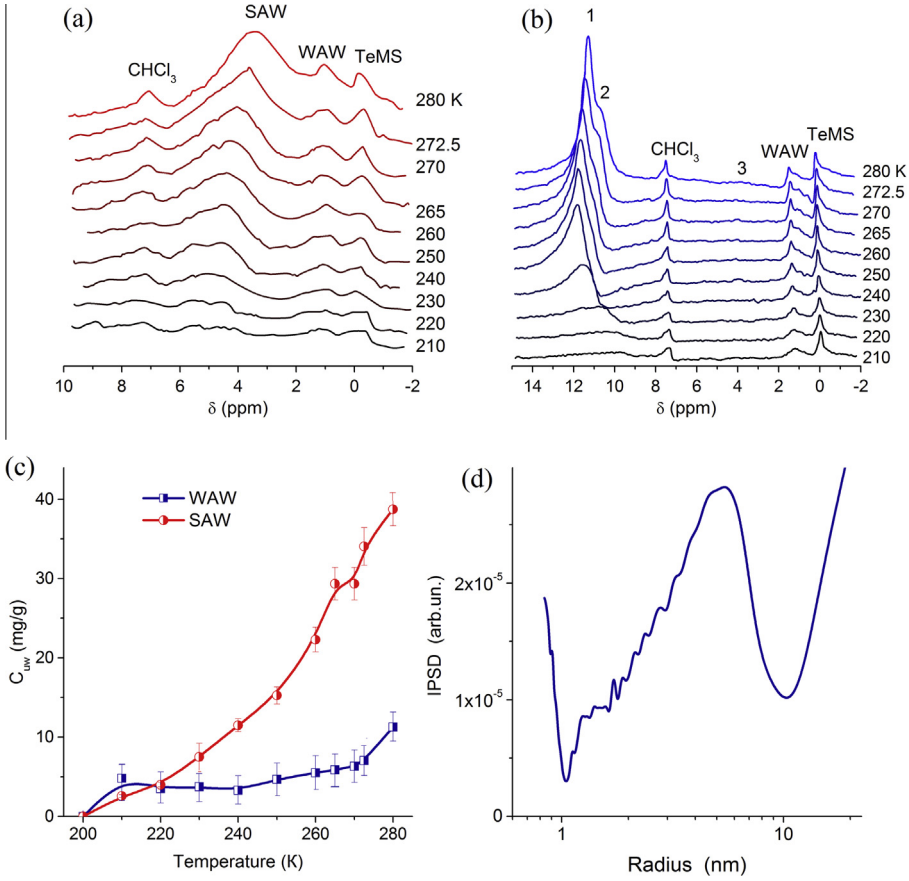

Fig. 10. ^{1}H NMR spectra recorded at different temperatures of water (h = 0.05 g/g) bound to HS2 in the $CDCl_3$ dispersion medium (a) without and (b) with addition of TFAA (15 wt.% with respect to $CDCl_3$ amount), (c) amounts of SAW and WAW vs. temperature without TFAA, and (d) size distribution of water structures without TFAA.

several types of SAW, which can dissolve acids or salts differently [29,65,66]. Typically, interfacial WAW cannot dissolve the acids. Here trifluoroacetic acid (TFAA) was added to chloroform-*d* medium (C_{TFAA} = 15 wt.% in $CDCl_3$). Before addition of TFAA, bound water is observed as SAW at 3.5 ppm at 280 K and 5 ppm at 210 K, as well as WAW at δ_H = 1.0–1.5 ppm (Fig. 10a and c). The intensity of the SAW signal decreases more rapidly than the WAW signal (Fig. 10c). Besides these signals of interfacial water, signals of $CHCl_3$ (as an admixture in $CDCl_3$) and tetramethylsilane (as a chemical shift standard added to $CDCl_3$) are also observed.

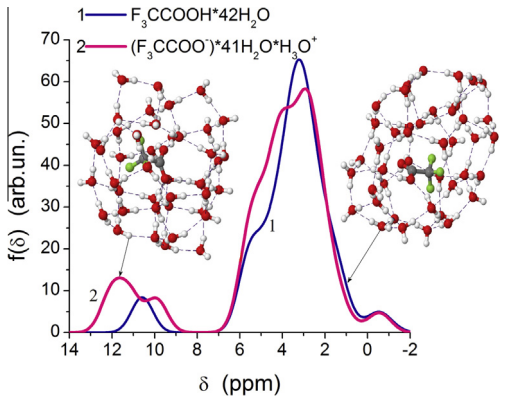

Fig. 11. ^{1}H NMR spectra of hydrated TFAA in molecular (curve 1) or ionized (curve 2) state calculated with GIAO/B3LYP/6-31G(d,p)//HF/6-31G(d,p).

From comparison of the ^{1}H NMR spectra of water bound to HS2 without (Fig. 6a) and with $CDCl_3$ (Fig. 10a), a disordering of SAW is observed due to the weakly polar liquid dispersion medium. Evidence of disordering comes from δ_H values being smaller in the presence of $CDCl_3$, and the SBW amount decreases from 0.035 g/g to 0.023 g/g. This is due to the displacement of a portion of bound water from the silica surface by $CDCl_3$ (Table 2, *S*, *V*) leading to a decrease in the γ_S value, and an increase in $\langle T \rangle$. Despite the low water content (h = 0.05 g/g), several types of water structures including nanoclusters at R < 1 nm, larger clusters (R = 1–10 nm) and domains (R > 10 nm) are observed (Fig. 10d, Table 2).

Addition of TFAA results in significant downfield shifts of SAW signals (δ_H = 12–13 ppm) due to fast proton exchange between TFAA and water molecules (Fig. 10b). At T > 240 K, two SAW signals (signals 1 and 2, Fig. 10b) corresponding to different amounts of dissolved TFAA (more dissolved TFAA for water with signal 1) are observed. Besides SAW with TFAA, a weak signal of SAW without dissolved TFAA (signal 3) is observed at 4 ppm. At 273–250 K, signal 2 decreases more than signal 1, and a downfield shift is observed for signals 1 and 2. But at T < 250 K, an upfield shift is observed in parallel to a strong decrease in signal intensity due to freezing of both TFAA and water. Besides signals of SAW, signals from WAW at 1.0–1.5 ppm are observed (Fig. 10b). The chemical shift of WAW is the same with and without TFAA suggesting that WAW does not dissolve TFAA.

Theoretical calculations of the ^{1}H NMR spectra (GIAO/DFT) of hydrated TFAA in molecular and ionized states (Fig. 11) suggest that signals 1 and 2 (Fig. 10b) may be caused by hydrated TFAA in similar states.

4. Conclusion

Despite partial hydrophobization (heterogenization resulting in a mosaic surface with hydrophilic and hydrophobic patches) of the PS300 surface by attachment of TMS groups (Θ_{TMS} = 37.2%), modified silica can bind significant amounts of water (up to ~5 g/g) in an aqueous suspension. However, only approximately 0.5 g/g of this water is strongly bound while the major fraction of water is weakly bound. The presence of surface TMS groups causes the appearance of weakly associated water (at chemical shift δ_H = 1–2 ppm) at the interfaces, even in the aqueous suspension of TMS-silica.

The adsorption of methane onto partially silylated nanosilica with pre-adsorbed water (0.05 g/g) increases with temperature in contrast to the adsorption of methane onto unmodified silica where a reduction of methane adsorption is seen with increasing temperature. It is believed that changes in both confined space effects and the temperature dependent organization of interfacial water may explain these results.

Changes in the organization of interfacial water are observed upon changes in the types of dispersion media and co-adsorbates. In weakly polar $CDCl_3$ medium, interfacial water exists in states that are strongly (chemical shift δ_H = 4–5 ppm) and weakly (δ_H = 1–2 ppm) associated, as well as strongly (changes in the Gibbs free energy $-\Delta G$ > 0.5–0.8 kJ/mol) and weakly ($-\Delta G$ < 0.5–0.8 kJ/mol) bound. Water in these different forms results in differences in their activity as solvents. For instance, WAW does not dissolve trifluoroacetic acid, but some SAW can dissolve TFAA. In addition the SAW activity differs for different fraction of SAW (e.g., located in narrower and broader pores). This appears as downfield and upfield shifts of water/TFAA clusters and domains with temperature. Therefore, the increase in the adsorption of methane onto partially silylated nanosilica with increasing temperature can be explained by enhanced mobility of unfrozen water which is displaced from some narrow pores, and these pores can be occupied by methane.

Acknowledgments

The authors are grateful to European Community, Seventh Framework Programme (FP7/2007–2013), Marie Curie International Research Staff Exchange Scheme (IRSES Grant No. 612484) for financial support. The authors thank Dr. E.F. Voronin for sample preparation.

References

[1] M. Inagaki, F. Kang, M. Toyoda, H. Konno, Advanced Materials Science and Engineering of Carbon, Elsevier, Amsterdam, 2014.
[2] T.A. Semelsberger, Chemical carriers, in: Reference Module in Chemistry, Molecular Sciences and Chemical Engineering, Fuels – Hydrogen Storage, 2009, pp. 504–518.
[3] D.J. Durbin, C. Malardier-Jugroot, Int. J. Hydrogen Energy 38 (2013) 14595–14617.
[4] J.P. Marco-Lozar, M. Kunowsky, J.D. Carruthers, Á. Linares-Solano, Carbon 76 (2014) 123–132.
[5] A. Policicchio, E. Maccallini, R.G. Agostino, F. Ciuchi, A. Aloise, G. Giordano, Fuel 104 (2013) 813–821.
[6] Y. Yao, D. Liu, S. Xie, Int. J. Coal Geol. 131 (2014) 32–40.
[7] A.R. Vélez, Comput. Mater. Sci. 50 (2011) 1016–1021.
[8] K.A. Rahman, W.S. Loh, K.C. Ng, Procedia Eng. 56 (2013) 118–125.
[9] L. Ding, A.O. Yazaydin, Micropor. Mesopor. Mater. 182 (2013) 185–190.
[10] G.-Q. Kong, Z.-D. Han, Y. He, S. Ou, W. Zhou, T. Yildirim, R. Krishna, C. Zou, B. Chen, C.-D. Wu, Chem. Eur. J. 19 (2013) 14886–14894.
[11] J. Moellmer, A. Moeller, F. Dreisbach, R. Glaeser, R. Staudt, Micropor. Mesopor. Mater. 138 (2011) 140–148.
[12] Y. Wang, C. Tan, Z. Sun, Z. Xue, Q. Zhu, C. Shen, Y. Wen, S. Hu, Y. Wang, T. Sheng, X. Wu, Chem. Eur. J. 20 (2014) 1341–1348.
[13] Z. Meng, R. Lu, D. Rao, E. Kan, C. Xiao, K. Deng, Int. J. Hydrogen Energy 38 (2013) 9811–9818.
[14] G. Ning, H. Wang, X. Zhang, C. Xu, G. Chen, J. Gao, Particuology 11 (2013) 415–420.
[15] M. Fujiwara, Y. Fujio, H. Sakurai, H. Senoh, T. Kiyobayashi, Chem. Eng. Process. Process Intensif. 79 (2014) 1–6.
[16] E. Acha, J. Requies, M.B. Güemez, V.L. Barrio, J.F. Cambra, P.L. Arias, Int. J. Hydrogen Energy 39 (2014) 5257–5266.
[17] M. Tagliabue, G. Bellussi, P. Broccia, A. Carati, R. Millini, P. Pollesel, C. Rizzo, Chem. Eng. J. 210 (2012) 398–403.
[18] S. Xu, Y. Luo, B. Tan, Macromol. Rapid Commun. 34 (2013) 471–484.
[19] G. Garberoglio, R. Vallauri, Micropor. Mesopor. Mater. 116 (2008) 540–547.
[20] M.K. Antoniou, A. Policicchio, K. Dimos, D. Gournis, M.A. Karakassides, R.G. Agostino, Micropor. Mesopor. Mater. 158 (2012) 332–338.
[21] J. Keypour, A.H. Asl, A. Rashidi, Chem. Eng. J. 183 (2012) 510–514.
[22] S.B. Kalidindi, R.A. Fischer, Phys. Status Solidi 250 (2013) 1119–1127.
[23] M. Klell, H. Eichlseder, M. Sartory, Int. J. Hydrogen Energy 37 (2012) 11531–11540.
[24] G. Cipriani, V. Di Dio, F. Genduso, D. La Cascia, R. Liga, R. Miceli, G. Ricco Galluzzo, Int. J. Hydrogen Energy 39 (2014) 8482–8494.
[25] H.P. Veluswamy, R. Kumar, P. Linga, Appl. Energy 122 (2014) 112–132.
[26] A. Ding, L. Yang, S. Fan, X. Lou, Chem. Eng. Sci. 96 (2013) 124–130.
[27] S. Eyer, N.P. Stadie, A. Borgschulte, L. Emmenegger, J. Mohn, Adsorption 20 (2014) 657–666.
[28] C. Horch, S. Schlayer, F. Stallmach, J. Magn. Reson. 240 (2014) 24–33.
[29] V.M. Gun'ko, V.V. Turov, Nuclear Magnetic Resonance Studies of Interfacial Phenomena, CRC Press, Boca Raton, 2013.
[30] I.I. Salame, T.J. Bandosz, J. Colloid Interface Sci. 210 (1999) 367–374.
[31] J.K. Brennan, T.J. Bandosz, K.T. Thomson, K.E. Gubbins, Colloids Surf. A: Physicochem. Eng. Aspects 187–188 (2001) 539–568.
[32] V.V. Turov, A.A. Turova, E.V. Goncharuk, V.M. Gun'ko, Appl. Surf. Sci. 255 (2008) 3310–3317.
[33] V.M. Gun'ko, V.V. Turov, V.M. Bogatyrev, A.Y. Petin, A.V. Turov, V.V. Trachevskyi, J.P. Blitz, Appl. Surf. Sci. 258 (2011) 1306–1316.
[34] V.M. Gun'ko, V.V. Turov, R.L.D. Whitby, G.P. Prykhod'ko, A.V. Turov, S.V. Mikhalovsky, Carbon 57 (2013) 191–201.
[35] V.M. Gun'ko, V.V. Turov, V.M. Bogatyrev, B. Charmas, J. Skubiszewska-Zięba, R. Leboda, S.V. Pakhovchishin, V.I. Zarko, L.V. Petrus, O.V. Stebelska, M.D. Tsapko, Langmuir 19 (2003) 10816–10828.
[36] V.M. Gun'ko, V.V. Turov, V.I. Zarko, E.V. Goncharuk, I.I. Gerashchenko, A.A. Turova, I.F. Mironyuk, R. Leboda, J. Skubiszewska-Zięba, W. Janusz, J. Colloid Interface Sci. 308 (2007) 142–156.
[37] V.M. Gun'ko, V.V. Turov, R. Leboda, J. Skubiszewska-Zięba, B. Charmas, Adsorption 19 (2013) 305–321.
[38] V.M. Gun'ko, V.V. Turov, R. Leboda, V.I. Zarko, J. Skubiszewska-Zięba, B. Charmas, Langmuir 23 (2007) 3184–3192.
[39] V.M. Gun'ko, E.F. Voronin, L.V. Nosach, V.V. Turov, Z. Wang, A.P. Vasilenko, R. Leboda, J. Skubiszewska-Zięba, W. Janusz, S.V. Mikhalovsky, J. Colloid Interface Sci. 355 (2011) 300–311.
[40] V.M. Gun'ko, G.R. Yurchenko, V.V. Turov, E.V. Goncharuk, V.I. Zarko, A.G. Zabuga, A.K. Matkovsky, R. Leboda, J. Skubiszewska-Zięba, W. Janusz, G.J. Phillips, S.V. Mikhalovsky, J. Colloid Interface Sci. 348 (2010) 546–558.
[41] S. Subramanian, E.D. Sloan Jr., Fluid Phase Equilib. 158–160 (1999) 813–820.
[42] L. Ballard, E.D. Sloan Jr., Fluid Phase Equilib. 216 (2004) 257–270.
[43] E.F. Vansant, P. Van Der Voort, K.C. Vrancken, Characterization and Chemical Modification of the Silica Surface: Studies in Surface Science and Catalysis, 93, Elsevier, Amsterdam, 1995.
[44] V.P. Glushko (Ed.), Handbook of Thermodynamic Properties of Individual Substances, Nauka, Moscow, 1978 (in Russian).
[45] J. Mitchell, J.B.W. Webber, J.H. Strange, Phys. Rep. 461 (2008) 1–36.
[46] R. Kimmich, NMR Tomography, Diffusometry, Relaxometry, Springer, Heidelberg, 1997.
[47] O.V. Petrov, I. Furó, Progr. NMR Spectrosc. 54 (2009) 97–122.
[48] R.J. Hunter, Zeta Potential in Colloid Sciences, Academic Press, London, 1981.
[49] M.J. Frisch, G.W. Trucks, H.B. Schlegel, G.E. Scuseria, M.A. Robb, J.R. Cheeseman, G. Scalmani, V. Barone, B. Mennucci, G.A. Petersson, H. Nakatsuji, M. Caricato, X. Li, H.P. Hratchian, A.F. Izmaylov, J. Bloino, G. Zheng, J.L. Sonnenberg, M. Hada, M. Ehara, K. Toyota, R. Fukuda, J. Hasegawa, M. Ishida, T. Nakajima, Y. Honda, O. Kitao, H. Nakai, T. Vreven, J.A. Montgomery, Jr., J.E. Peralta, F. Ogliaro, M. Bearpark, J.J. Heyd, E. Brothers, K.N. Kudin, V.N. Staroverov, T. Keith, R. Kobayashi, J. Normand, K. Raghavachari, A. Rendell, J.C. Burant, S.S. Iyengar, J. Tomasi, M. Cossi, N. Rega, J.M. Millam, M. Klene, J.E. Knox, J.B. Cross, V. Bakken, C. Adamo, J. Jaramillo, R. Gomperts, R.E. Stratmann, O. Yazyev, A.J. Austin, R. Cammi, C. Pomelli, J.W. Ochterski, R.L. Martin, K. Morokuma, V.G. Zakrzewski, G.A. Voth, P. Salvador, J.J. Dannenberg, S. Dapprich, A.D. Daniels, O. Farkas, J.B. Foresman, J.V. Ortiz, J. Cioslowski, D.J. Fox, Gaussian 09, Revision D.01, Gaussian Inc., Wallingford CT, 2013.
[50] J.J.P. Stewart, MOPAC 2012, Colorado Springs, CO: Stewart Computational Chemistry, USA, 2014, <http://openmopac.net/>.
[51] J.D.C. Maia, G.A.U. Carvalho, C.P. Mangueira Jr., S.R. Santana, L.A.F. Cabral, G.B. Rocha, J. Chem. Theory Comput. 8 (2012) 3072–3081.
[52] E.F. Pettersen, T.D. Goddard, C.C. Huang, G.S. Couch, D.M. Greenblatt, E.C. Meng, T.E. Ferrin, J. Comput. Chem. 25 (2004) 1605–1612.
[53] G.A. Zhurko, D.A. Zhurko, Chemcraft (version 1.7, build 382), 2014, <http://www.chemcraftprog.com>.
[54] Jmol: an open-source Java viewer for chemical structures in 3D (version 14.2.2), 2014, <http://www.jmol.org/>.
[55] R.K. Iler, The Chemistry of Silica, Wiley, Chichester, 1979.

[56] A.P. Legrand (Ed.), The Surface Properties of Silicas, Wiley, New York, 1998.
[57] A.V. Kiselev, V.I. Lygin, Infrared Spectra of Surface Compounds, Wiley, New York, 1975.
[58] M.L. Hair, Infrared Spectroscopy in Surface Chemistry, Dekker, New York, 1967.
[59] B. McCool, L. Murphy, C.P. Tripp, J. Colloid Interface Sci. 295 (2006) 294–298.
[60] V.M. Gun'ko, D.J. Sheeran, S.M. Augustine, J.P. Blitz, J. Colloid Interface Sci. 249 (1) (2002) 123–133.
[61] V.M. Gun'ko, V.I. Zarko, R. Leboda, E. Chibowski, Adv. Colloid Interface Sci. 91 (2001) 1–112.
[62] M. Chaplin, Water Structure and Science, <http://www.lsbu.ac.uk/water/> (24.05.14).
[63] D.R. Kinney, I.-S. Chaung, G.E. Maciel, J. Am. Chem. Soc. 115 (1993) 6786–6794.
[64] J.A. Pople, W.G. Schneider, H.J. Bernstein, High-Resolution Nuclear Magnetic Resonance, McGraw-Hill Book Company, New York, 1959.
[65] V.M. Gun'ko, L.P. Morozova, A.A. Turova, A.V. Turov, V.E. Gaishun, V.M. Bogatyrev, V.V. Turov, J. Colloid Interface Sci. 368 (2012) 263–272.
[66] V.M. Gun'ko, V.V. Turov, V.I. Zarko, E.M. Pakhlov, A.K. Matkovsky, O.I. Oranska, B.B. Palyanytsya, O.S. Remez, Y.M. Nychiporuk, Y.G. Ptushinskii, R. Leboda, J. Skubiszewska-Zięba, Colloids Surf. A: Physicochem. Eng. Aspects 456 (2014) 261–272.